PRACTICAL CHALLENGES AND FAILURE MODES DURING FABRICATION OF HAYNES 230 MICRO-PIN SOLAR RECEIVERS FOR HIGH TEMPERATURE SUPERCRITICAL CARBON DIOXIDE OPERATION

Patrick S. McNeff
Oregon State University
Corvallis, OR, USA

Brian K. Paul
Oregon State University
Corvallis, OR, USA

Ömer N. Doğan
National Energy
Technology Laboratory
Albany, OR, USA

Kyle A. Rozman
Leidos Research Support Team
Pittsburgh, PA, USA

Sean Kissick
Oregon State University
Corvallis, OR, USA

Hailei Wang
Utah State University
Logan, UT, USA

M. Kevin Drost
Oregon State University
Corvallis, OR, USA

Brian M. Fronk*
Oregon State University
Corvallis, OR, USA
Brian.Fronk@oregonstate.edu

ABSTRACT

Printed circuit heat exchangers (PCHX) fabricated from high nickel alloys have shown promise as primary heat exchangers, recuperators, and solar receivers for high temperature and pressure supercritical carbon dioxide power cycles. There are numerous challenges in fabricating these devices including forming channel features, joining via diffusion or transient liquid phase bonding, and brazing/welding of headers. Commercial entities are understandably hesitant to share propriety best practices, and both commercial and non-commercial entities working on these components tend not to publically share failures and mistakes. However, sharing of this information could prevent similar costly errors and further the understanding of the coupled manufacturing, materials and mechanics issues in creating these components.

Thus, in this paper, we document the challenges, failures, and mitigation methods uncovered in fabrication of prototype micro-pin based solar thermal receivers constructed of Haynes 230 and fabricated through a combination of photochemical machining (PCM), wire electrical discharge machining (EDM), transient liquid phase (TLP) bonding, vacuum brazing, and gas tungsten arc welding (GTAW). The receiver is designed to absorb concentrated solar fluxes greater than 140 W cm^{-2}, while heating supercritical carbon dioxide from 550 °C to 720 °C at a pressure of 20 MPa to 25 MPa. The prototype receiver consists of a thin ($\sim$ 450 μm), Haynes 230 coversheet bonded to a 15 cm × 15 cm Haynes 230 micro-pin plate. The pieces are joined using a TLP bonding process with a nickel-phosphorus interlayer. Prior to bonding, micro-pins with height $\sim$150 μm and diameter 300 μm are fabricated using PCM in the plate, and through slot features are made using wire EDM. Finally, flow headers are joined to the microchannel plate through a combination of vacuum brazing and GTAW.

During hydrostatic proof testing, the prototype device failed when the coversheet delaminated from the pin array at a pressure of 290 bar. A failure analysis including scanning electron microscopy (SEM) to view failure sites and energy-dispersive X-ray spectroscopy (EDS) to evaluate elemental analysis of the failed areas was conducted. The failure modes can be broadly categorized as (1) failures potentially relating to reliquification of the transient liquid phase bonds between the micro-pins plate and coversheet during post-processing, (2) failures related to manufacturing defects, and (3) failures attributed to design.

INTRODUCTION

The United State Department of Energy (DOE) has identified supercritical carbon dioxide (sCO$_2$) Brayton cycles with turbine inlet temperatures >720 °C as the most promising power cycle for next generation concentrated solar thermal power (CSP) systems [1]. In these systems, a field of two-axis tracking heliostats concentrate solar radiation on to a receiver located atop a central tower. The concentrated thermal energy is then transferred to the sCO$_2$ power system or to thermal storage through a circulating gas, liquid molten salt, or through solid particles [1].

In ongoing work by the authors, we are developing a solar receiver technology that uses concentrated solar flux greater than 140 W cm^{-2} to heat sCO$_2$ from an inlet temperature of 550 °C to an outlet of 720 °C at an operating pressure of > 20 MPa. The receiver must have an efficiency greater than 90%, meaning that for every 1 MW of concentrated solar flux incident on the surface, 900 kW of energy is transferred into the sCO$_2$. This efficiency is inclusive of optical reflection losses, reradiation losses, and convective losses from the receiver surface. Gas based solar receivers (air, helium, etc.) are typically constructed of multiple tubes in parallel/circuited flow arrangement to

---
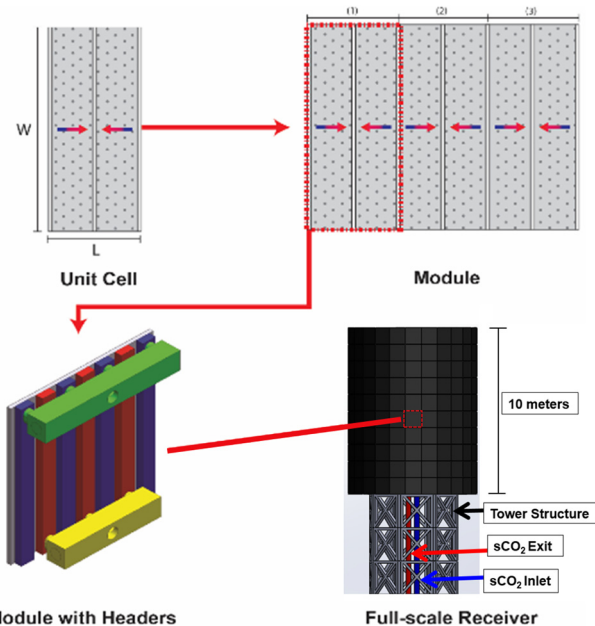
Figure 1: Conceptual schematic of numbering-up concept.

minimize pressure drops. However, the gas-side convective heat transfer coefficient is relatively low, resulting in high receiver surface temperature and unacceptable thermal losses [2]–[4]. Furthermore, using high pressure sCO_2 in a tubular receiver would require thick walled tubes, further increasing thermal resistance and surface temperature.

Thus, we have pursued a micro-pin ($D_H \sim 300$ μm) concept to meet the challenges of high temperature/pressure operation and the need for extremely high gas-side convective heat transfer coefficients. Micro-pins were chosen over microchannels as they are more resistance to plugging and provide better flow distribution. A blocked microchannel could result in local overheating and failure of the device.

This technology allows incident fluxes greater than 140 W cm^{-2} with efficiency > 90%, and the use of very thin walls to contain the pressures. Figure 1 shows a conceptual schematic of how micro-pin based receivers could be numbered-up to multi-MW central receivers. Here, multiple-parallel unit-cells are fabricated into modules (~ 1 m × 1 m), which are then arranged into a central receiver and plumbed in parallel. Supercritical CO_2 from the main receiver riser is split into each module, and then further subdivided into each unit-cell where it is heated, recombined in the outlet headers and sent back to the power cycle/thermal storage. This approach minimizes parasitic pressure drop of the sCO_2 [5], enables the possibility of zoned flow control within the receiver to maximize annualized performance [6], and allows for the realization of economies of scale in the manufacturing of the individual modules.

The goal of our ongoing work is to demonstrate the ability to fabricate and test a scaled prototype (15 cm × 15 cm, approximately 15 kW of thermal input) in a concentrated solar dish. The prototype consists of multiple unit-cells and is designed to heat sCO_2 to temperatures of 720 °C using concentrated solar flux. Materials, mechanical, and thermal computational and experimental studies [5], [7]–[11] were used to specify designs and fabrication techniques that would meet the performance targets and survive the extreme conditions. This paper describes the challenges, failure modes, and opportunities for improvements from the initial attempt to synthesize these separate effects investigations into the design and fabrication of a prototype unit.

RECEIVER MATERIAL AND DESIGN

To survive the extreme operating conditions, only nickel-based solid-solution-strengthened and precipitation-strengthened superalloys were considered. After considering (a) the availability of material in the required form factor (sheet, plate, and bar), (b) the corrosion resistance with sCO_2 at temperature and pressure, (c) the ease of fabricating micro features, and (d) our experience with diffusion and transient-liquid phase bonding of the materials, we selected Haynes 230, a solid-solution-strengthened alloy. First, although Haynes 230 is primarily a solid-solution-strengthened alloy, it contains high volume fraction of M6C phase, which is instrumental in stabilizing matrix grain size at high bonding temperatures. Haynes 230 is known as one of the most grain-growth-resistant materials in the solid-solution-strengthened superalloys family. Second, Haynes 230 is one of the most corrosion-resistant alloys at high temperatures. Third, we had prior bonding experience with this alloy. Finally, we were able to demonstrate excellent channel depth tolerances using sinker electrical discharge machining (EDM) (±0.7%) and photochemical machining (PCM) (±3.9%) using Haynes 230, as well as identify vendors that could scale these processes to a 1 m × 1 m scale.

With this material as the basis, a conceptual rendering of a single unit-cell within the prototype is shown in Figure 2. Each unit-cell consists of a thin, flat, coversheet coated with a high absorptivity material (Figure 2a). The inside of the unit-cell consists of a flow passage containing a staggered array of micro-pins (detailed schematic shown in Figure 3). The flow length of a unit-cell is determined by the maximum allowable pressure drop within the device. As shown in Figure 2b, each unit-cell consists of two inlet headers (from the left and right), and a central outlet header. Supercritical CO_2 enters from both sides, is

Table 1: Dimensions of unit-cell and pin array.

Variable Name	Dimension	Value
t	Coversheet thickness	450 μm
L	Unit-cell base length	5 cm
W	Unit-cell base width	15 cm
D_{pin}	Pin diameter	300 μm
h_{pin}	Pin height	150 μm
S_L	Longitudinal pitch	520 μm
S_T	Transverse pitch	600 μm
S_D	Diagonal pitch	600 μm
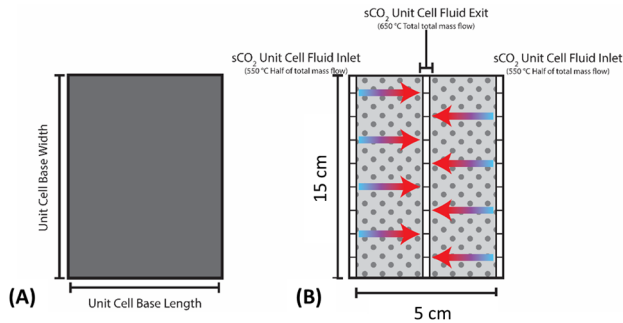
Figure 2: Schematic of unit-cell with representative dimensions (a) with bonded coversheet on and (b) coversheet removed showing internal pins and sCO_2 flow paths.
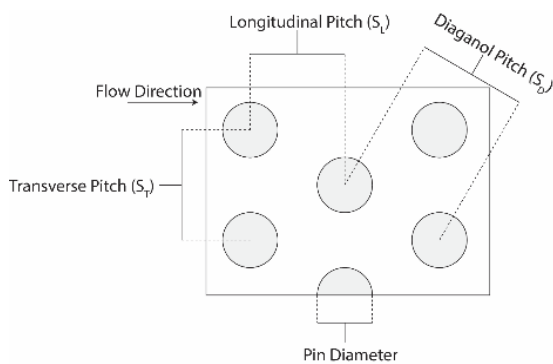
**Figure 3:** Detailed schematic of micro-pin array.

heated to the desired outlet temperature, and leaves through the middle. The dimensions for the unit-cell and staggered pin-array in the prototype device are provided in Table 1.

The prototype module consists of three unit-cells in parallel (Figure 4). Figure 4a shows a top view of the three-unit-cell prototype with the coversheet removed. Figure 4b shows the backside of this pin array with flow distribution headers and Figure 4c-d shows the cross section of the unit-cell and module headers with important dimensions. Flow enters through the module inlet header (in green) from the main receiver riser. The sCO_2 is distributed to the four unit-cell inlet headers (in blue), and then exits each unit-cell through the three unit-cell outlet headers (in red). Finally, flow from each unit-cell outlet header is collected in a module outlet header (in yellow), and returned to the main receiver downcomer. The dimensions for the prototype unit headers are shown in Table 2.

Table 2: Dimensions of unit-cell and module headers.

Header	W (mm)	L (mm)	D (mm)	t (mm)
(A) Unit-cell header	8.125	16.25	6.25	5
(B) Module header	22.7	22.7	12.7	5

Finally, penetrations were made through the micro-pin plate to allow sCO_2 to flow between the micro-pin array and the unit-cell inlet/outlet headers, shown conceptually in Figure 5. The
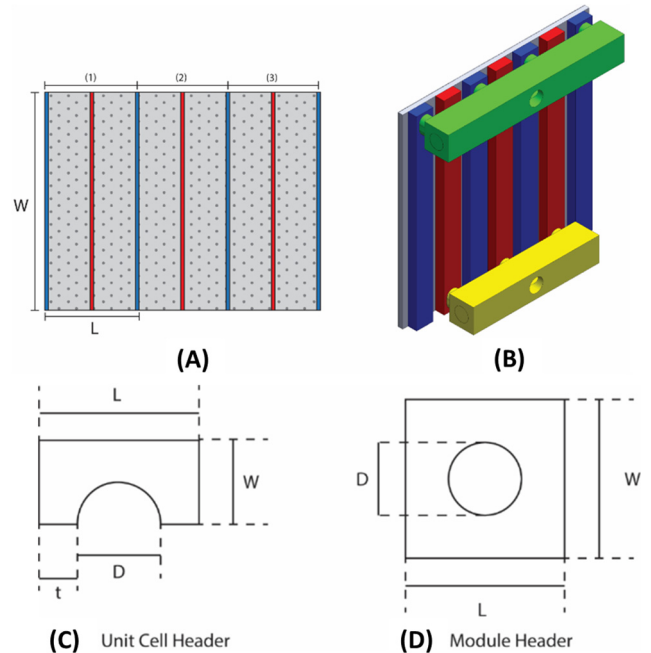
Figure 4: Schematic of three unit-cell prototype (a) with coversheet removed (b) unit cell and module headers shown and (c-d) header cross section with dimensions.
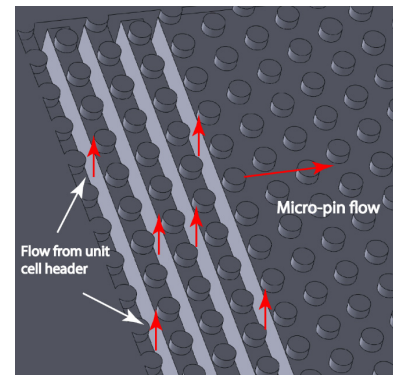

Figure 5: Rendering of the inlet/outlet slits for transition of flow from unit-cell headers to micro-pin array.

width of these slits was 0.20 mm, and the length was 10 mm. They were staggered from the top of the unit-cell to the bottom to enable flow to be well distributed.

RECEIVER FABRICATION APPROACH

A process flow diagram for the fabrication of the prototype receiver is shown in Figure 6. Raw material inputs are shown in green. First, a hot-rolled plate of Haynes 230 with a thickness of 6.35 mm was cut to size (~ 15 cm × 15 cm) and then the micro-pin array design was etched using a vendor proprietary photochemical etch process (Step **1** in Figure 6). An example of etched pin-array is shown in Figure 7. Then, the plate was sent to a second vendor for a wire EDM of the 0.2 wide mm slits (Step **2**). A graphite punch was used to create a through hole to thread
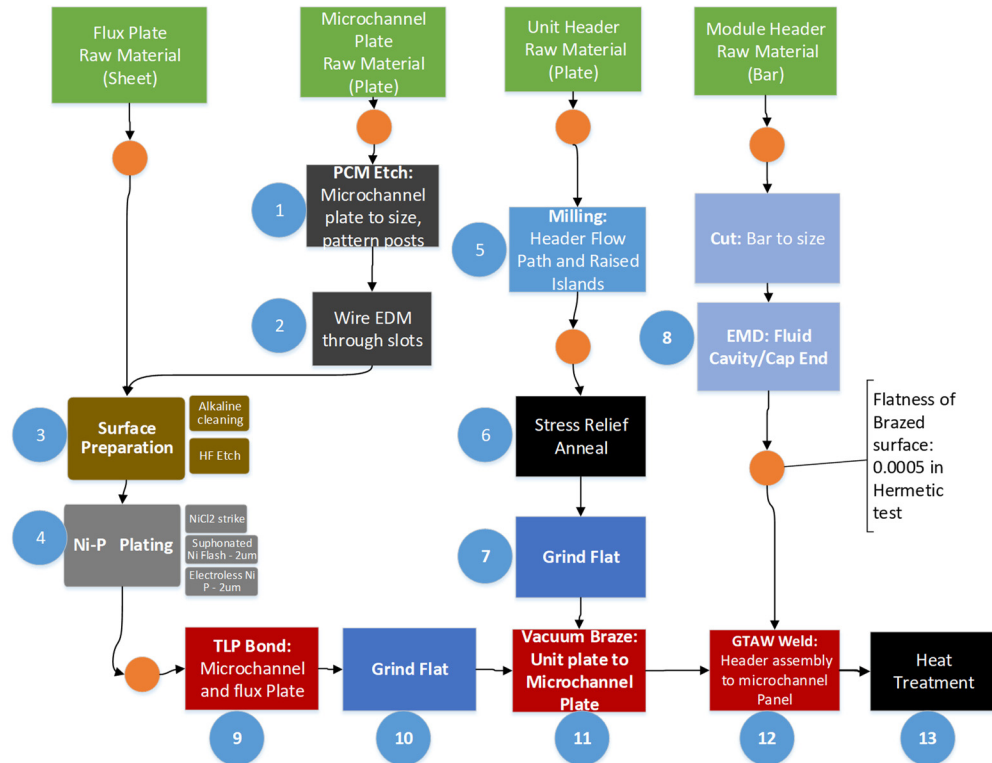
Figure 6: Process flow diagram for fabrication of prototype receiver.

the cutting wire. Each staggered slit required a new through hole to be made.

Then, a 450 μm thick sheet of cold-rolled Haynes 230 was cut to size for the receiver coversheet. The micro-pin plate and cover sheet bonding surfaces were prepared with an alkaline cleaning and hydrofluoric acid etch (**3**). The treated surfaces were then joined using a transient liquid phase bonding process (**9**). Here, the parts are subjected to a high temperature and pressure. The faying surfaces are plated with a material that contains a melting point depressant (in this case, phosphorous), causing the joint to liquefy at high temperature. Then, the melting point depressant diffuses into the base metal, resulting in an isothermal solidification of the joint. Initially, a NiCl strike was applied to help increase adhesion. Then, a 2 μm sulfonated layer of pure nickel was electrically deposited, followed by a 2 μm electroless mid-phosphorus layer (~6% P). This resulted in a phosphorous content of approximately 3% in the interlayer. The bonding temperature was 1150 °C at a vacuum pressure less than 1×10^{-5} torr for a dwell time of 4 hours. Once bonding was complete, the combined part was ground flat on the faying surface for the unit-cell headers.

In parallel, the unit-cell header plate was milled out of hot-rolled Haynes 230 plate to achieve the dimensions shown in Table 2, previously. Rather than individual parts as shown conceptually in Figure 4, a single plate was used that contained all the unit-cell headers with inlet/outlet ports (Figure 8). After machining, the part was stress relief annealed at 1200 °C for 1 hour (3 °C per minute ramp up/down), and ground flat. The unit-

cell header plate was then joined to the micro-pin plate via a vacuum brazing process (Table 3) using a 50 μm nickel based brazing foil containing boron as a melting point depressant (MBF-51 in [12]).

Finally, the module headers were machined from Haynes 230 bar and joined to the unit-cell header plate via a gas tungsten arc welding (GTAW) process. GTAW was also used to repair an external leak from the TLP process, and to join a set of Haynes 230 tubes for pressure testing. The entire part was shown to be hermetic to a shop air test of approximately 0.76 MPa. A photograph of the complete prototype receiver is shown in Figure 8.

Table 3: Vacuum brazing parameters.

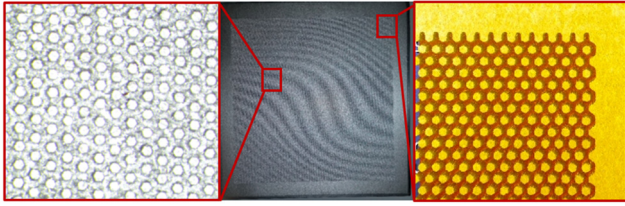| Step	Description	Purpose
1	Ramp to 950 °C @ 5 °C per minute	
2	1st Hold: 950 °C for 1.5 hours	Ensure part evenly heated
3	2nd Hold: 1195 °C for 2.5 hours	Liquefy braze and diffuse away boron and silicon
4	Cool to 1100 °C (2 °C per min) in 1.5 mbar Argon	Solidify braze for diffusion hold
5	3rd Hold: 1100 °C for 3.5 hours	Diffuse away any residual boron or silicon

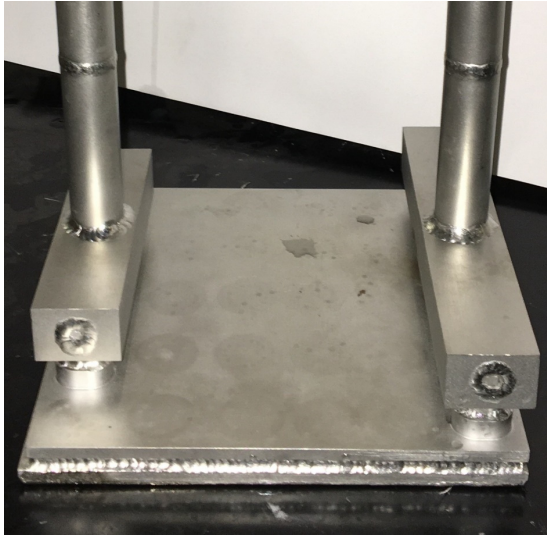**Figure 7:** Example of etched pins.

Figure 8: Complete receiver prototype.

PROOF TESTING AND FAILURE ANALYIS

Prior to installing the prototype on-sun, a room temperature proof test was conducted using the standards outlined in ASME Section VIII Div. 1 Hydrostatic Pressure Testing - Article UG-99(b). The hydrostatic test pressure was determined from Equation 1.

$$P = 1.3 \cdot MAWP \cdot \frac{\sigma_T}{\sigma_D} \qquad (1)$$

where *MAWP*, σ_T, and σ_D are the maximum allowable working pressure/design pressure (20 MPa), the allowable stress at test temperature (20 °C), and the ASME maximum allowable stress at design temperature (720 °C). For Haynes 230 at these temperatures, the values of σ_T and σ_D were determined to be 207 MPa and 65 MPa, respectively [13]. This resulted in a room temperature required proof pressure testing of 82.8 MPa. The testing procedure is based on the ASME guidelines, summarized in Figure 9.

After confirming the unit showed no external leakage with air at 0.76 MPa, the unit was connected to a manual hydraulic pump and filled with hydraulic oil. The first step in the test required pressure to reach 33 MPa. The unit was ramped up to 33 MPa by first increasing pressure to 10 MPa, holding a minute, increasing pressure to 20 MPa, waiting a minute, and then increasing pressure to 33 MPa. During the last ramp to 33 MPa,

the unit failed at approximately 29 MPa. Failure occurred when the coversheet produced a bulge due to separation from the micro-pins (Figure 10). No external leakage occurred during the failure event.

The bulged area shown in Figure 10 was removed via laser cutting (Figure 11a), cleaned in an ultrasonic acetone bath, and sectioned using wire EDM (Figure 11b). We then conducted detailed scanning electron microscopy (SEM) to view failure sites and energy-dispersive X-ray spectroscopy (EDS) to evaluate elemental analysis of the failed areas. Analysis was conducted of the top coversheet, and the micro-pin plate in the failed region. This analysis revealed several potential failure modes that can be broadly categorized as (1) failures potentially relating to the transient liquid phase bonds between the micro-pins and 0.45 mm coversheet during post-processing, (2) failures related to manufacturing defects, (3) failures attributed to design. Each are described below, followed by some suggestions for mitigation of the failures that may be of use to the sCO$_2$ community fabricating high temperature/pressure heat exchangers based on printed circuit type architectures.
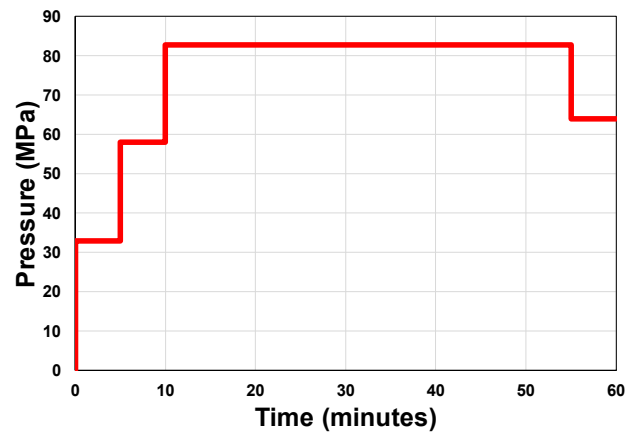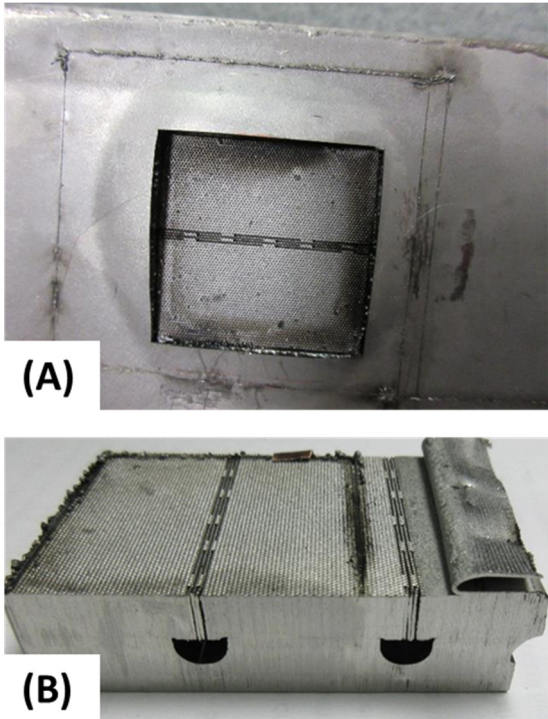

Figure 9: Proof pressure testing operating specifications.

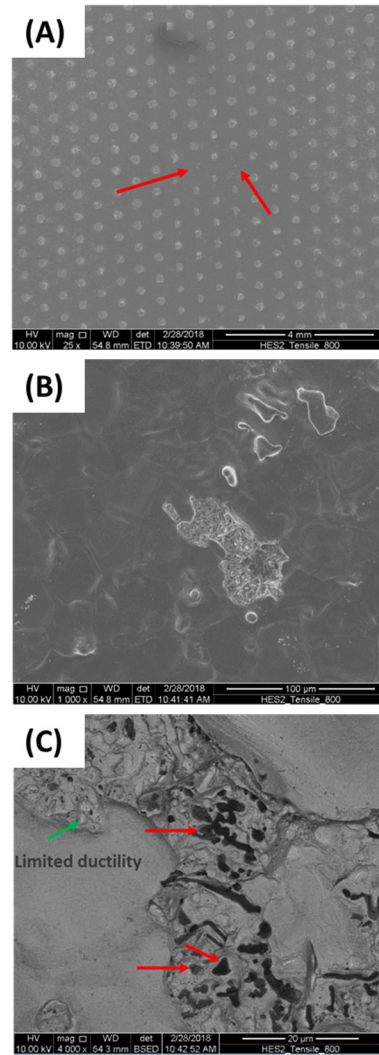**Figure 10:** Photograph of coversheet bulge failure.

Figure 11: (a) Top view of coversheet showing bulge section removed and (b) side view of section micro-pin plate.

Figure 12: SEM of bottom side of coversheet showing (a) regions where not all pins were adhered (b) close up of "missing" pin area showing limited bonding and (c) backscatter image of "missing" pin area showing dark Al-oxide regions (red arrows) and areas of limited ductility (green arrow).

Failures Related to TLP Bond

In general, the SEM analysis showed that the fracture took place in the bond region in a ductile manner. Notably, the failure appears to be centered over the series of slits in the micro-pin array which function as fluid inlet/outlets (Figure 11a). Within the failed region, some pins were not adhered, or were poorly adhered to the top plate (Figure 12a-b). These "missing" bonded pins were sporadically located, and likely not the sole cause of failure. In regions where pins were partially adhered, aluminum oxide particles were found using EDS, causing a local brittle failure (Figure 12c). For pins that were well adhered, Al-oxide was found in the periphery of the bond, causing local brittle failure, despite a general ductile failure in the center (Figure 13). In both the well and poorly adhered pins, voids within the bonding region were detected (Figure 14). Finally, the profiles of both the adhered and poorly adhered pins show "liquid-like" wavy solidification features (see Figure 14) that are inconsistent with the original smooth photochemical etching process.

All of these findings support a hypothesis that failure was at least in part due to the TLP bond re-liquefying during the high temperature vacuum brazing and post-processing (heat treatment process). In this prototype, phosphorous was used as the melting point depressant based on prior work at Oregon State University. Phosphorous is much slower to diffuse than the more industry standard boron used in many TLP process. If all of the phosphorous did not diffuse out during the bonding process, then

during the brazing or heat treatment process, the coversheet may lift off the pins or slide (article was not horizontal), causing the observed sporadic attachment and voids/inclusions. Furthermore, a liquefied bond would be much more susceptible to oxygen diffusion, resulting in the formation of Al-oxide within the bonding area of poorly adhered pins, and at the periphery of the well bonded

Failure Related to Manufacturing Defects

The fluid inlet/outlet slits are machined in the micro-pin plate using a wire-EDM process, as discussed above. The through hole for insertion of the wire is made with a graphite-based tool. SEM images of the pins near the slits show that some
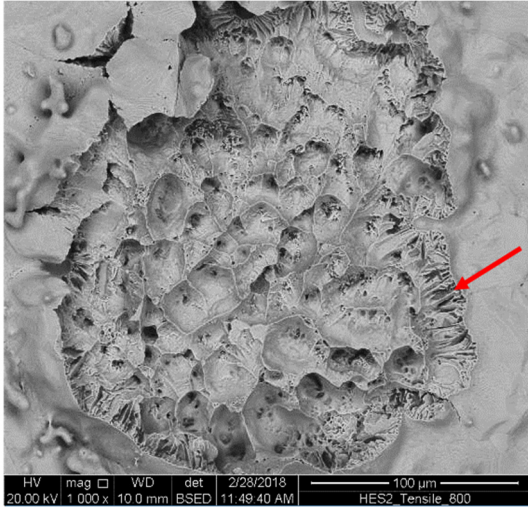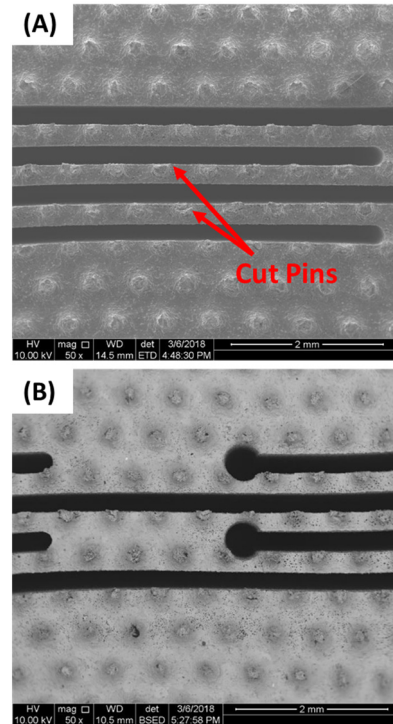
Figure 13: SEM of bottom side of coversheet showing failure of a well adhered pin with Al-oxide (dark spots) in bond periphery and local brittle failure.
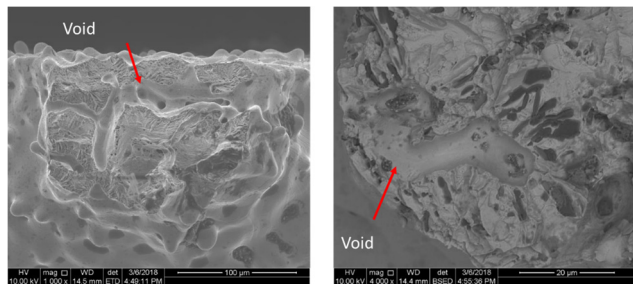
Figure 14: Observed voids in bond region of (left) poorly adhered pin and (right) well adhered pin.

Figure 15: Image showing (a) cut pins and (b) potential carbon contamination (dark spots) in vicinity of wire EDM slit.

pins are cut due to misregistration of the wire, reducing the cross section and bonding area (Figure 15). Furthermore, carbon contamination near the slits was observed (dark color in Figure 15b), attributed to the graphite hole punching tool. The carbon contamination was not removed by the cleaning process prior to electroplating and TLP bonding process, potentially altering the TLP bonding process. The probability of the contribution of both of these factors to the failure is increased due to the apparent initiation of failure in the region of the fluid inlet/outlet slits, shown in Figure 11a.

During the failure analysis there was some concern that the micro-pin array may have been over etched during the PCM process, yielding smaller than expected pins. This concern was due to the small pin cross sectional area observed in the failed regions as shown in Figure 15a. However, we analyzed the pin geometries in a region without failure by machining away the thin coversheet to reveal the pins, shown in Figure 16a. Here, the pin spacing and diameter are as expected (Table 1). Thus, the observed decreased area in the failed region is believed to be from necking of the pins during failure.
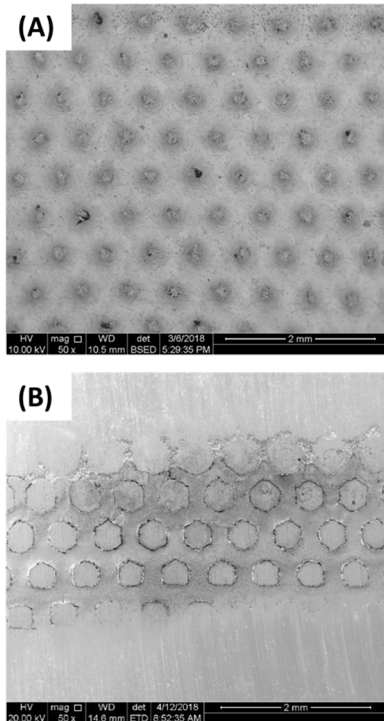
Failures Related to Design

We identified the inability of the design to accommodate manufacturing defects related to the TLP bonding and wire EDM processes as a key failure mode. The use of micro-pins versus continuous microchannels allows the device to be resilient to plugging. In a solar application, if even a single channel were plugged, a hot spot could develop leading to failure. To specify the geometry of the pin array design, the primary constraints were mechanical, manufacturing, and hydraulic.

The target lifetime of the solar receiver is >10,000 cycles. The type of failure observed in the proof test (i.e., coversheet delimiting from micro-pin array) was identified as the most critical potential failure mode to address. To develop a design to avoid this, elasto-plastic properties of TLP joined samples of Haynes 230 with patterned features similar to those of the prototype were obtained at room temperature and operational temperature of 760 °C. The data were then used to calibrate a FEA model of the joint, where the yield strength of the bond layer was iteratively changed and resulting force-displacement simulations compared to the data [9]. It was found that the joint materials' elastoplastic behavior was similar to that of the base material. Using these elastoplastic properties, FEA was performed for a range of micro-pin geometries (spacing and diameter) to detect the onset of plastic failure at 25 MPa and material properties at operation temperature (from [13]). The FEA model used to examine the deformation of the micro-pin included a bottom plate, pins, and a top plate, as well as a bonded region between the top plate and the pins. A pressure of 25 MPa
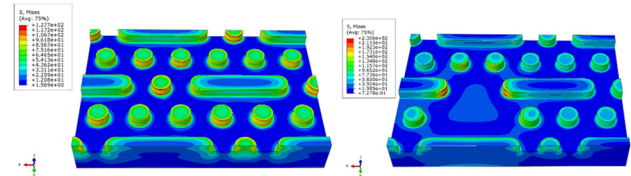
Figure 16: Image showing top view (a) of failed pin array with decreased pin diameter and (b) pin diameter in region without failure.

Figure 17: Image showing top view (a) of failed pin array with decreased pin diameter and (b) pin diameter in region without failure.

observed failure indicates that a more defect tolerant design of the pin array would increase the likelihood of prototype success. Many other sCO$_2$ recuperator and primary heat exchanger printed-circuit type designs fabricated with similar methods use micro channels with continuous walls rather than micro-pins. This increases the area available for bonding and increases the resilience of the device to manufacturing defects. However, this comes at the cost of decreased resilience to channel plugging and flow maldistribution, which is unacceptable for concentrated solar applications. Some alternatives are discussed below.

LESSONS LEARNED AND CONCLUSIONS

Fabricating high temperature and pressure heat exchangers is challenging and expensive, and the subject of multiple ongoing efforts across the world. The extreme operating conditions of the concentrated solar thermal environment make the problem even more challenging. This paper presented details on the design, fabrication, and identified failure modes in a printed-circuit type heat exchanger. From the challenges presented above, a few lessons learned can be of value to the sCO$_2$ community working with high-nickel content alloys.

Joining: One of the key failure mechanisms was related to the joining process. Joining of nickel-based alloys is widely studied in the literature. Generally, these studies are done with carefully controlled tensile test articles, and not with full components. As shown here, there can be difficulties when scaling proven laboratory processes to actual devices. Based on prior success of transient liquid phase bonding Haynes 230 with a Ni-P interlayer in 5 cm and 8 cm scale devices [15], the approach was adopted here, with approximately 3% P as a melting point depressant within the interlayer. Transient liquid phase bonding has the positive aspect that the bond region liquefies and can potentially fill some surface defects during the bonding process. However, due to the relatively slow diffusion of phosphorous into the base metal, there is some concern that the bond in the prototype device may have become liquid during other processes, causing degradation in the bond. Boron will diffuse faster than phosphorus, which would help ensure isothermal solidification of the joint during bonding. However, there is the possibility that because it diffuses so fast, uneven heating of large parts during the thermal ramp to the bonding temperature could cause the melting point depressant to non-uniformly diffuse out of some regions of the part before it is at the desired temperature.

To retire these risks, we have moved to a solid-state diffusion bonding process for Haynes 230. Here, the interlayer

was applied to all interior surfaces. Potential designs were then limited to geometric combinations that would remain elastic. The avoidance of plastic failure would also prevent failure of the joint via low-cycle fatigue, i.e., > 10,000 cycle life.

When fabricating the pins with PCM, the pin-to-pin span/height ratio was approximately 2. This, combined with the mechanical model results specified the geometric limits of the pin array. With these limits, computational fluid dynamics simulations were used to evaluate the thermal hydraulic performance of the prototype unit-cells with different pin geometries and unit-cell flow length, as described in Hyder and Fronk [5]. These analysis considered axial conduction through coversheet, radiation and reflection losses for different optical coatings, and convection losses for different ambient conditions. The thermal analysis was confirmed with lab-scale experimental data from [14]. The design targets were a receiver efficiency > 90% (with assumed optical coating) and pressure loss less than 0.4 MPa, while heating 20 to 25 MPa sCO$_2$ from 550°C to 720°C. The pin-array dimensions reported in Table 1 met these targets with a mechanical safety factor > 1.2 at operating temperature using conservative mechanical properties of Haynes 230 [13].

However, over the 15 cm × 15 cm area of the prototype device, there are approximately 125,000 pins. Thus, even for highly controlled manufactured processes, there is a relatively high statistical likelihood that one or more pins may not be fabricated to tolerance, bonded correctly (Figure 12), and/or damaged during other fabrication process (Figure 15). The

and bond region will remain solid throughout the diffusion bonding process and, therefore, surface features have a more pronounced effect on porosity along the bond line. Based on the work of Kapoor et al. [16] for diffusion bonding of Haynes 230, we have identified process parameters (temperature, pressure, time) that will provide high percent bonded area without significant creep, permitting us to move forward with a solar receiver prototype design based on solid-state diffusion bonding. In our preliminary work exploring this approach, we are considering sub-scale prototypes either with or without a pure nickel-layer, with promising initial results in terms of joint yield strength and percent bonded area. Our second generation prototype will be fabricated using a diffusion bonding process.

Design: Another key lesson is to develop designs that are resilient to manufacturing defects, particularly when fabricating many small micro features. In our first prototype design, the failure of one pin potentially caused a cascade of failures resulting in "unzipping" of the bonded coversheet from the micro-pin array, as observed. In the failure analysis, some poorly bonded pins due were observed, although it was not possible to identify one single pin as the initiation of the failure. To mitigate this, we are considering designs consisting of arrays of pins and short bars (Figure 17). This type of design maintains resistance to plugging and blocking of the flow, while also increasing the area available for bonding. FEA analysis shows that this two feature design is more resilient to "missing" pins or bond area defects than a pure pin array. Work is ongoing to identify the best statistical distribution of defects to assess the resilience of the design.

In sum, we hope that the challenges, failure modes and lessons learned presented here can be used by others in the sCO_2 field to develop designs and fabrication strategies for their own applications that have a higher probability of success. Ultimately, this will decrease the time and cost in moving sCO_2 technology from the laboratory to the field.

NOMENCLATURE
D_{pin} pin height (µm)
h_{pin} pin height (µm)
L unit-cell base length (cm)
$MAWP$ max allowable working pressure (MPa)
P pressure (MPa)
S_D diagonal pitch (µm)
S_L longitudinal pitch (µm)
S_T transverse pitch (µm)
t coversheet thickness (µm)
W unit-cell base width (cm)
σ_D allowable stress at design temperature (MPa)
σ_T allowable stress at test temperature (MPa)

ACKNOWLEDGEMENTS

REFERENCES
[1]   M. Mehos, C. Turchi, J. Vidal, M. Wagner, Z. Ma, C. Ho, W. Kolb, C. Andraka, and A. Kruizenga, "Concentrating Solar Power Gen3 Demonstration Roadmap," 2017.

[2]   M. Romero, R. Buck, and J. E. Pacheco, "An Update on Solar Central Receiver Systems, Projects, and Technologies," *J. Sol. Energy Eng.*, vol. 124, no. 2, p. 98, 2002.

[3]   C. K. Ho and B. D. Iverson, "Review of high-temperature central receiver designs for concentrating solar power," *Renew. Sustain. Energy Rev.*, vol. 29, pp. 835–846, 2014.

[4]   C. K. Ho, "Advances in central receivers for concentrating solar applications," *Sol. Energy*, 2017.

[5]   M. B. Hyder and B. M. Fronk, "Simulation of thermal hydraulic performance of multiple parallel micropin arrays for concentrating solar thermal applications with supercritical carbon dioxide," *Sol. Energy*, vol. 164, no. February, pp. 327–338, 2018.

[6]   K. R. Zada, M. B. Hyder, M. Kevin Drost, and B. M. Fronk, "Numbering-Up of Microscale Devices for Megawatt-Scale Supercritical Carbon Dioxide Concentrating Solar Power Receivers," *J. Sol. Energy Eng.*, vol. 138, no. 6, p. 061007, 2016.

[7]   T. L'Estrange, "Experimental Characterization of a Supercritical Carbon Dioxide Microchannel Solar Thermal Reciever," Cambridge University Press, Corvallis, OR, 2015.

[8]   M. Kapoor, Ö. N. Doğan, C. S. Carney, R. V. Saranam, P. McNeff, and B. K. Paul, "Transient-Liquid-Phase Bonding of H230 Ni-Based Alloy Using Ni-P Interlayer: Microstructure and Mechanical Properties," *Metall. Mater. Trans. A*, vol. 48, no. 7, pp. 3343–3356, Jul. 2017.

[9]   W. H. Pratte, "Computational Modeling of a Diffusion Bonded Microchannel under High Pressure and Temperature," Oregon State University, 2017.

[10]   C. Rymal, A. V. Apte, V. Narayanan, and K. Drost, "Numerical Design of a High-Flux Microchannel Solar Receiver," in *Proceedings of the ASME 2013 7th International Conference on Energy Sustainability*, 2013, p. V001T11A012.

[11]   Ö. N. Doğan, C. Carney, R. P. Oleksak, C. R. Disenhof, and G. R. Holcomb, "High-Temperature Corrosion of Diffusion Bonded Ni-based Superalloys in CO2," in *The 5th International Symposium - Supercritical CO2 Power Cycles*, 2016.

[12]   Metglas, "Amorphous Brazing Foil," 2018. [Online]. Available: https://metglas.com/wp-content/uploads/2018/10/Metglas-Brazing-Foil-Brochure-2018-FINAL.pdf. [Accessed: 24-Apr-2019].

[13]   Haynes International, "Haynes ® 230 ® alloy," 2017. [Online]. Available: http://haynesintl.com/docs/default-source/pdfs/new-alloy-brochures/high-temperature-

alloys/brochures/230-brochure.pdf.

[14] T. L'Estrange, E. Truong, C. Rymal, E. Rasouli, V. Narayanan, S. Apte, and K. Drost, "High Flux Microscale Solar Thermal Receiver for Supercritical Carbon Dioxide Cycles," in *ASME 2015 13th International Conference on Nanochannels, Microchannels, and Minichannels*, 2015, p. V001T03A009.

[15] V. Narayanan, B. M. Fronk, T. L'Estrange, and E. Rasouli, "Supercritical Carbon Dioxide Solar Thermal Power Generation—Overview of the Technology and Microchannel Receiver Development," 2019, pp. 333–355.

[16] M. Kapoor, Ö. N. Doğan, K. Rozman, J. Hawk, A. Wilson, T. L'Estrange, and V. Narayanan, "Diffusion bonding of H230 Ni-superalloy for applicatoin in microchannel heat exhangers," in *The 5th International Symposium - Supercritical CO2 Power Cycles*, 2016.

DuEPublico

Duisburg-Essen Publications online